

# Hydrodynamic Limit of the Inhomogeneous $\ell$ -TASEP with Open Boundaries: Derivation and Solution

Dan D. Erdmann-Pham<sup>1</sup>, Khanh Dao Duc<sup>2</sup>, and Yun S. Song<sup>2,3,4,\*</sup>

<sup>1</sup>Department of Mathematics, University of California, Berkeley, CA 94720, USA

<sup>2</sup>Computer Science Division, University of California, Berkeley, CA 94720, USA

<sup>3</sup>Department of Statistics, University of California, Berkeley, CA 94720, USA

<sup>4</sup>Chan Zuckerberg Biohub, San Francisco, CA 94158

\*To whom correspondence should be addressed: yss@berkeley.edu

March 15, 2018

## Abstract

The totally asymmetric simple exclusion process, which describes the transport of interacting particles in a lattice, has been actively studied over the past several decades. For general cases where particles have an extended size and hop at site-dependent rates, however, theoretically analyzing the dynamics has remained elusive. Here, we present such an analysis by deriving and solving the hydrodynamic limit. We obtain closed-form formulas for steady-state particle densities and currents, as well as phase transition boundaries. Surprisingly the latter depend on only four parameters: the particle size and the first, the last, and the minimum hopping rates. Our results agree well with Monte Carlo simulations and can be used in inference.

## 1 Introduction

Since its introduction [1, 2], the totally asymmetric simple exclusion process (TASEP) has been widely used to model transport phenomena in non-equilibrium particle systems. Many mathematicians and physicists have studied this stochastic process under various conditions motivated by a broad range of applications. In biology, for example, the TASEP has been used to describe and infer various cellular processes ranging from molecular transport along the cytoskeleton [3–5] to gene expression dynamics associated with transcription and translation ([6–15], to name a few). In particular, to realistically model the process of translation, a generalized version of the TASEP called the inhomogeneous  $\ell$ -TASEP needs to be employed. In this model, each particle occupies  $\ell \in \mathbb{N}$  sites and the hopping rate can vary along the lattice, hence generalizing various TASEP models studied in the past few decades [7, 16, 17, 17–25]. Quantitative studies of this generalized model have mostly been limited to numerical simulations or mean-field approximations [7, 16–18, 23] that often rely on restricting the heterogeneity of rates to a small number of sites [17, 23].

Among the many methods developed to investigate the TASEP, a common approach is to study the continuum limit of the observed particle density, obtained in the large lattice size and small lattice spacing limit [26–30]. Analysis of this regime, called the hydrodynamic limit, involves a nonlinear partial differential equation (PDE), which in the classical TASEP case turns out to be the well-known Burgers’ equation [31]. Interestingly, for the inhomogeneous  $\ell$ -TASEP, a rigorous derivation of the hydrodynamic limit and subsequent analysis to determine the associated phase diagram are still missing.

Our goal here is to derive and solve the hydrodynamic limit of the inhomogeneous  $\ell$ -TASEP.

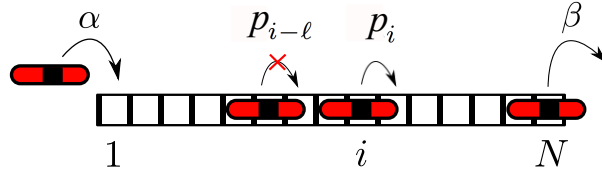


**Fig. 1: Illustration of the inhomogeneous  $\ell$ -TASEP with open boundaries.** Particles (of size  $\ell = 3$  here) enter the first site of the lattice at rate  $\alpha$  and a particle at position  $i$  (here defined by the position of the midpoint of the particle) moves one site to the right at rate  $p_i$ , provided that the next  $\ell$  sites are empty. A particle at the end of the lattice exits at rate  $\beta$ .

Upon finding a general PDE satisfied by the density of particles, we provide a complete characterization of the phase diagram associated with the stationary solution. In particular, we show that the boundaries of the phase diagram depend only on four parameters of the model: the particle size, and the first, the last, and the minimum hopping rates in the hydrodynamic limit. For each region of the phase diagram, we obtain closed-form formulas for the flux and site-specific particle density, and show that they agree well with Monte Carlo simulations. Lastly, we discuss how our results can be used in various contexts and examples arising from the past literature, and suggest a novel method for inferring rates.

## 2 The inhomogeneous $\ell$ -TASEP with open boundaries

### 2.1 Model description

First we briefly introduce the inhomogeneous  $\ell$ -TASEP on a one-dimensional lattice with  $N$  sites. In this process, each particle is of a fixed size  $\ell \in \mathbb{N}$  and is assigned a common reference point (e.g., the midpoint in the example illustrated in **Fig. 1**). The position of a particle is defined as the location of its reference point on the lattice. A configuration of particles is denoted by the vector  $\tau = (\tau_1, \dots, \tau_N)$ , where  $\tau_i = 1$  if the  $i$ th site is occupied by a particle reference point and  $\tau_i = 0$  otherwise. The hopping rate at site  $i$  of the lattice is denoted by  $p_i > 0$ . During every infinitesimal time interval  $dt$ , each particle located at position  $i \in \{1, \dots, N - 1\}$  has probability  $p_i dt$  of hopping exactly one site to the right, provided that the next  $\ell$  sites are empty; particles at positions between  $N - \ell + 1$  and  $N$ , inclusive, never get obstructed. Additionally, a new particle enters site 1 with probability  $\alpha dt$  if  $\tau_i = 0$  for all  $i = 1, \dots, \ell$ . If  $\tau_N = 1$ , the particle at site  $N$  exits the lattice with probability  $\beta dt$ . We call the parameters  $\alpha$  and  $\beta$  the entrance and exit rates, respectively.

### 2.2 The hydrodynamic limit

In the special case of the homogeneous ( $p_i = p$  for all  $i$ ) 1-TASEP, the stationary distribution of the process decomposes into matrix product states, which can be treated analytically [32]. Unfortunately, in the general case this approach is intractable, necessitating alternative methods such as hydrodynamic limits. When  $\ell > 1$ , deriving the hydrodynamic limit is not straightforward, however, as the process does not possess stationary product measures [33]. To tackle this problem, we first map the  $\ell$ -TASEP to another interacting particle system called the zero range process (ZRP) and then derive its hydrodynamic limit from the associated master equation. Such an approach has been considered before, but only for homogeneous rates and unbounded lattices [33, 34]. Here, we generalize the hydrodynamic limit to the case of inhomogeneous rates, and find appropriate boundary conditions for the resulting PDE to account for the boundedness of the system. More

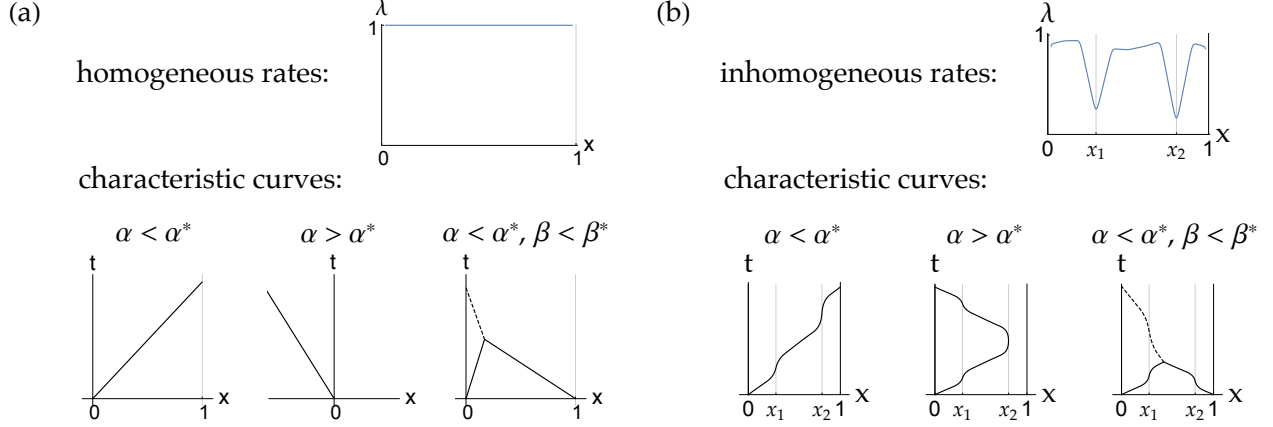


**Fig. 2: Characteristic curves.** Characteristic curves starting at lattice endpoints for different regions of the phase diagram. **(a)** Homogeneous rates give rise to straight line characteristics with speed  $\partial_\rho J(\rho_0)$  and  $\partial_\rho J(\rho_1)$ , respectively. **(b)** Inhomogeneous rates produce more complicated behavior, with characteristics curves slowing down (and potentially reversing direction) near the troughs ( $x_1$  and  $x_2$ ) of  $\lambda$ .

precisely, we obtain the hydrodynamic limit through the Eulerian scaling of time and space by a factor  $a \in O(N^{-1})$ , and by following its dynamics on scale  $x$  such that  $k = \lfloor \frac{x}{a} \rfloor$ , for  $1 < k < N$  [29]. Implementing this limiting procedure for the ZRP and mapping it back to the inhomogeneous  $\ell$ -TASEP, we find that the limiting occupation density  $\rho(x, t) = \mathbb{P}(\tau_k(t) = 1)$ , where  $k = \lfloor \frac{x}{a} \rfloor$ , satisfies the nonlinear PDE

$$\partial_t \rho = -\partial_x [\lambda(x) \rho G(\rho)] + \frac{a}{2} \partial_{xx} [\lambda(x) G(\rho)] + O(a^2), \quad (1)$$

where  $G(\rho) = \frac{1 - \ell \rho}{1 - (\ell - 1) \rho}$  and  $\lambda$  is a differentiable extension of  $(p_1, \dots, p_N)$ , such that  $\lambda(x) = \lambda(ka) = p_k$ . Details and relevant calculations are provided in the Appendix.

For the homogeneous 1-TASEP, the PDE (1) reduces to the well-known Burgers' equation, which can be established directly from the forward equation [31]. More generally, this PDE takes the form of a conservation law with systematic and diffusive currents  $J$  and  $J_D$ , given by

$$J(\rho, x) = \frac{\lambda(x) \rho (1 - \ell \rho)}{1 - (\ell - 1) \rho} \quad \text{and} \quad J_D(\rho, x) = \frac{\lambda(x) \rho}{1 - (\ell - 1) \rho}. \quad (2)$$

As  $a \ll 1$ , the systematic current dominates and solutions of (1) generically converge locally uniformly on  $(0, 1)$  to the so-called entropy solution of

$$\partial_t \rho = -\partial_x [\lambda(x) \rho G(\rho)], \quad (3)$$

which thus accurately captures the dynamics in the lattice interior (for boundary layer effects not reflected in (3), see the Appendix.) This first order nonlinear PDE can be solved using the method of characteristics [35]. Such analysis (which in the field of traffic flows has been developed independently as the theory of kinematic waves [36]) has previously been carried out for the homogeneous 1-TASEP [19, 27], where the characteristic curves turn out to be straight lines, and hence simple to understand (see **Fig. 2(a)**). The result is a phase diagram in  $\alpha$  and  $\beta$  that separates different regimes for the flux and density, in agreement with the one obtained from directly analyzing the

discrete process [37]. For inhomogeneous rates, however, the characteristic curves exhibit more complicated behavior, rendering the phase diagram analysis more challenging (see **Fig. 2(b)**). Surprisingly, we shall see that despite this added complexity, the phase diagram is exactly characterized by only a few statistics of the model.

### 2.3 The phase diagram

We now study the stationary solutions of (3) and look for a phase diagram describing the different regimes of the flux and particle density. We summarize here our main results and defer the details of the derivation to the Appendix. Without loss of generality, we embed the lattice into  $[0, 1]$ , and for ease of notation, define  $\lambda_0 = \lambda(0)$ ,  $\lambda_1 = \lambda(1)$ , and  $\lambda_{\min} = \min\{\lambda(x) : x \in [0, 1]\}$ .

The characteristics of (3) are solutions of the system of ordinary differential equations

$$\begin{aligned}\frac{dx^t}{dt} &= \lambda(x^t)H'(\rho^t), \\ \frac{d\rho^t}{dt} &= -\lambda'(x^t)H(\rho^t),\end{aligned}$$

where  $H(\rho) = \rho G(\rho)$ , and  $H'$  and  $\lambda'$  respectively denote the derivatives of  $H$  and  $\lambda$  with respect to their arguments. Initial information is propagated across space-time through the characteristics. Studying the stationary solutions of (3) thus requires evaluating the boundary densities from  $\alpha$  and  $\beta$ , and determining whether they are propagated into the lattice. Preservation of the current  $J$  throughout the system allows us to accomplish such evaluation by balancing currents across the lattice boundaries with interior currents. At  $x = 0$ , the result is an initial density  $\rho_0 := \rho(0)$ , given by

$$\rho_0 = \frac{\alpha}{\lambda_0 + (\ell - 1)\alpha}. \quad (4)$$

Studying the sign of  $\partial_\rho J$  shows that the characteristic curve associated with  $x = 0$  reaches  $x = 1$  (i.e.,  $\rho_0$  propagates into the system and fills it) if and only if  $\alpha < \alpha^*$ , where

$$\alpha^* = \frac{1}{2} \left[ \lambda_0 - \frac{\ell - 1}{(1 + \sqrt{\ell})^2} \lambda_{\min} - \sqrt{\left( \lambda_0 - \frac{\ell - 1}{(1 + \sqrt{\ell})^2} \lambda_{\min} \right)^2 - \frac{4\lambda_0 \lambda_{\min}}{(1 + \sqrt{\ell})^2}} \right], \quad (5)$$

and  $\beta$  is sufficiently large (see below). The corresponding critical current  $J$  assumed by the system is

$$J_L = \frac{\alpha(\lambda_0 - \alpha)}{\lambda_0 + (\ell - 1)\alpha}, \quad (6)$$

while the site-specific density is

$$\rho_L(x) = \frac{1}{2\ell} + \frac{J_L(\ell - 1)}{2\ell\lambda(x)} - \sqrt{\left( \frac{1}{2\ell} + \frac{J_L(\ell - 1)}{2\ell\lambda(x)} \right)^2 - \frac{J_L}{\ell\lambda(x)}}. \quad (7)$$

Determining densities at  $x = 1$  is more delicate, as a small exit rate can lead to particles lingering at the last site, splitting the density into two distinct branches [18]. As a result,  $\rho_1 := \rho(1)$  decomposes into the weighted average of two components

$$\rho_1^+ = \frac{\lambda_1 - \beta}{\lambda_1 + (\ell - 1)\beta} \quad \text{and} \quad \rho_1^- = \frac{\beta\rho_1^+}{\lambda_1}, \quad (8)$$

such that

$$\rho_1 = \frac{1}{\ell} \left( \frac{\rho_1^-}{\ell-1} + \rho_1^+ \right) = \frac{1}{\ell} \left( 1 - \frac{\beta}{\lambda_1} \right).$$

Similar to the left end of the lattice, we can find a critical value  $\beta^*$  for  $\rho_1$  to propagate through the lattice, and the associated current  $J_R$ . The formulas for  $\beta^*$  and  $J_R$  are identical to  $\alpha^*$  and  $J_L$ , respectively, except that  $\lambda_0$  needs to be replaced by  $\lambda_1$  and  $\alpha$  by  $\beta$  in (5) and (6). The associated site-specific density  $\rho_R$  is given by

$$\rho_R(x) = \frac{1}{2\ell} + \frac{J_R(\ell-1)}{2\ell\lambda(x)} + \sqrt{\left( \frac{1}{2\ell} + \frac{J_R(\ell-1)}{2\ell\lambda(x)} \right)^2 - \frac{J_R}{\ell\lambda(x)}}. \quad (9)$$

Note that the functional form of  $\rho_L$  differs from that of  $\rho_R$  mainly by the  $\pm$  sign in front of the square root, which accounts for the two different branches that appear when studying stationary solutions of (3). Based on their sign, we call the respective solutions the positive (or upper) branch and the negative (or lower) branch.

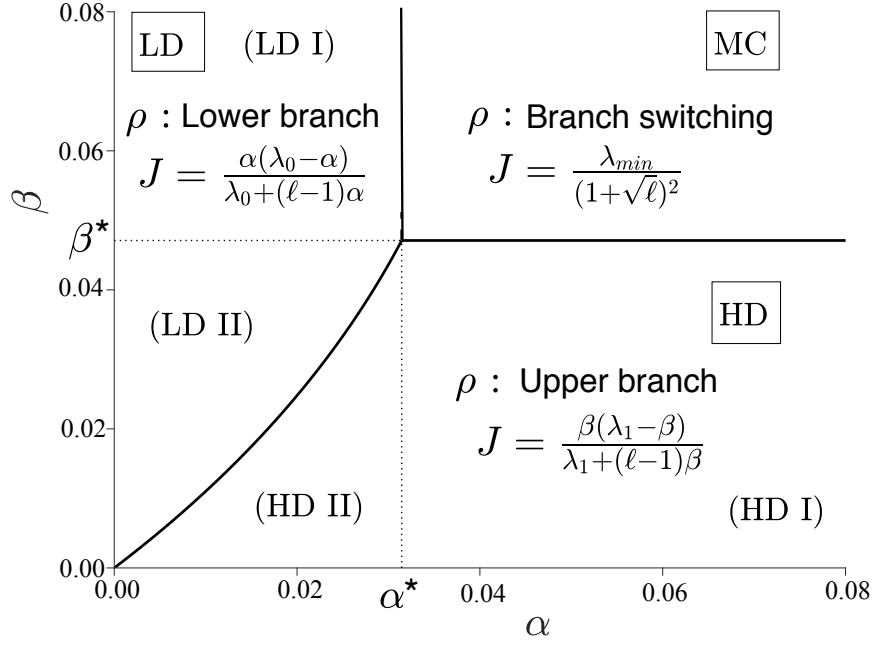
For a given rate function  $\lambda$ , we can now combine the above results to completely characterize the different phases of the system, as illustrated in **Fig. 3**, in terms of only  $\lambda_0$ ,  $\lambda_1$  and  $\lambda_{\min}$ :

1. *If  $\alpha < \alpha^*$  and  $\beta > \beta^*$ :* Only  $\rho_0$  fills the system, so  $\rho_L$  dominates. This is the low density (LD) I regime.
2. *If  $\alpha > \alpha^*$  and  $\beta < \beta^*$ :* Only  $\rho_1$  fills the system, so  $\rho_R$  dominates. This is the high density (HD) I regime.
3. *If  $\alpha < \alpha^*$  and  $\beta < \beta^*$ :* Both boundary characteristics propagate into the lattice and collide in the interior. Either characteristic carries low enough current to fill the system so the steady state is determined by the sign of the shock speed. It is positive if  $J_L > J_R$ , in which case  $\rho_L$  dominates (LD II regime), and negative if  $J_L < J_R$ , resulting in  $\rho_R$  to dominate (HD II regime).
4. *If  $\alpha > \alpha^*$  and  $\beta > \beta^*$ :* In this case neither characteristic fully fills the system, but rather propagates until  $x_{\min} = \arg \min_x \lambda(x)$ , where they reverse direction and return to their respective lattice ends. As each of them carries the maximum possible current (also referred to as the transport capacity of the system)

$$J_{\max} = \frac{\lambda_{\min}}{(1 + \sqrt{\ell})^2}, \quad (10)$$

this regime is called the maximal current (MC) regime. Assuming uniqueness of  $x_{\min}$ , this flow of characteristics describes the MC phase entirely. Its density is characterized by qualitatively different profiles left and right of  $x_{\min}$ : For  $x < x_{\min}$ ,  $\rho(x)$  is described by the upper branch (obtained by replacing  $J_R$  with  $J_{\max}$  in (9)), while for  $x > x_{\min}$ ,  $\rho(x)$  is described by the lower branch (obtained by replacing  $J_L$  with  $J_{\max}$  in (7)). That is, a branch switch occurs at  $x_{\min}$  (where  $\rho(x_{\min}) = (1 + \sqrt{\ell})^{-2}$ ). We proved more generally that every global minimum of  $\lambda$  regulates the traffic of particles (like a toll reducing the traffic flow) in this fashion: incoming densities to the left of it are always described by the upper branch whereas outgoing particles on the right follow the lower branch. Interestingly, this implies that in the case of multiple global minima, the density between two consecutive minima must undergo a discontinuous jump from lower to upper branch (for more details, see the Appendix)

(a) Phase diagram



(b)

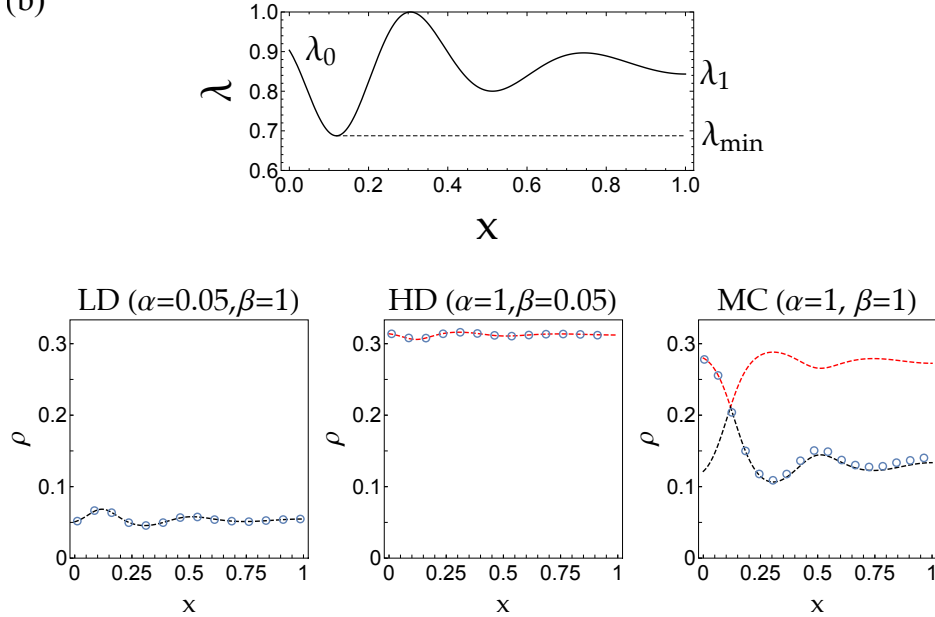


**Fig. 3: Phase diagram and density profiles.** (a) The phase diagram is completely determined by  $\lambda_0, \lambda_1, \lambda_{\min}$  and  $\ell$ . In this example,  $(\lambda_0, \lambda_1, \lambda_{\min}, \ell) = (0.9, 0.3, 0.1, 10)$ . All phase transitions are continuous in  $J$  and discontinuous in  $\rho$ . (b) Simulated results for  $\ell = 3$ ,  $N = 800$ , and the displayed  $\lambda$  are compared with theoretical predictions. Dashed black and red lines represent upper and lower branches of solutions to (1). Circles are averaged counts over  $5 \times 10^7$  Monte-Carlo steps after  $10^7$  burn-in cycles.

As shown in **Fig. 3(b)**, the densities predicted by our analysis agree well with Monte Carlo simulations in all regimes of the phase diagram. Our phase diagram generalizes the one obtained for the homogeneous 1-TASEP, as our results reduce to the known formulas [27] when  $\ell = 1$  and  $\lambda$  is constant. Interestingly, our analytic formulas for the flux and densities in the hydrodynamic limit are in agreement with recently published power series results for the discrete process in the special case of  $\alpha \ll \lambda_{\min}$  [14].

We highlight a few novel phenomena in our generalization: First, extending particles to size  $\ell > 1$  and lowering the limiting jump rate  $\lambda_{\min}$  reduces both the transport capacity  $J_{\max}$  and the critical rates ( $\alpha^*$  and  $\beta^*$ ) for entrance and exit, leading to an enlarged MC phase region. This is expected as fewer particles are needed to saturate the lattice, and distances between particles are larger, which in turn limits the number of particles able to cross a site per given time. This phenomenon is quantified precisely using our explicit expressions for  $\alpha^*$ ,  $\beta^*$ , and  $J_{\max}$  (see (5) and (10)).

Second, the inhomogeneity in  $\lambda$  may deform the LD-HD phase separation from being a straight line in the homogeneous  $\ell$ -TASEP [23] to a generally nonlinear curve (see **Fig. 3(a)**) determined by solutions  $(\alpha, \beta)$  of

$$\frac{\alpha(\lambda_0 - \alpha)}{\lambda_0 + (\ell - 1)\alpha} = \frac{\beta(\lambda_1 - \beta)}{\lambda_1 + (\ell - 1)\beta},$$

corresponding to the condition  $J_L = J_R$ . This is a consequence of  $\alpha$  and  $\beta$  affecting the system at different scales whenever  $\lambda_0 \neq \lambda_1$ , resulting in a phase diagram that is no longer symmetric.

Lastly, our observation of density profiles performing branch switching in the MC phase was indiscernible in the homogeneous case, as the high density and low density branches merge into a single value (viz.  $\rho = \frac{1}{\sqrt{\ell+1}}$ ).

### 3 Examples and applications

In what follows, we consider some examples and applications of our analysis, and show how previous results and studies fit within our framework.

#### 3.1 Example 1: Bottleneck induced by defect sites

Due to its relevance in applications and mathematical tractability, many studies of the TASEP have considered inhomogeneity created by defects, i.e., sites with lower rates. In the simplest case of a single defect, mean-field approximations successfully approximated the phase diagram and density profiles [16, 17, 19–21, 24]. Compared to the homogeneous system, the main effect is an enlarged MC phase region with a decrease of the maximal current. Moreover, at the defect site the density profiles in the MC phase exhibit a separation between a region of high density on the left, and low density on the right. For macroscopic clusters of defect sites, refined mean-field approaches have shown that these effects persist [23, 25]. Using the hydrodynamic limit, we are able to recover these results precisely: Defining  $\lambda(x) = 1 - \eta_\varepsilon(x)$ , where  $\eta_\varepsilon$  is a suitably normalized bump function centered around the bottleneck  $x_0$ , we find that with  $\lambda_{\min} = \lambda(x_0) < 1$ ,

$$\alpha^* = \beta^* = \frac{1}{1 + \sqrt{\ell}} \left( 1 - \sqrt{1 - \lambda_{\min}} \right),$$

$$J_{\max} = \frac{\lambda_{\min}}{(1 + \sqrt{\ell})^2},$$

leading to the aforementioned reduction in transport capacity and shifts in the phase diagram. The co-existence of low and high density regions in the MC phase is reflected in the branch switching

phenomenon.

### 3.2 Example 2: Linear rate function

Monotonically-varying jump rates are another simple example of spatial inhomogeneity. This kind of pattern has been observed in translation dynamics, where hopping rates increase on average [11, 38, 39]. Such variation can be modeled to first approximation by a linear rate function  $\lambda(x) = s(x-1) + 1$  for  $s \in [0, 1]$  (the case of decreasing rates with  $s < 0$  can be treated analogously). With  $\lambda_{\min} = \lambda_0 = 1 - s$  and  $\lambda_1 = 1$ , we can compute  $\alpha^*$  and  $\beta^*$  from (5). For the particular case of  $\ell = 1$ ,

$$\alpha^* = \frac{1-s}{2} \quad \text{and} \quad \beta^* = \frac{1}{2} \left( 1 - \sqrt{s} \right).$$

The LD and HD regions are then separated by the curve

$$\alpha(1 - \alpha - s) = \beta(1 - \beta)(1 - s),$$

recovering previous results obtained through mean-field approximations [22]. Since  $\lambda$  achieves its minimum at the lattice entry site, both LD and MC profiles are described by the lower branch, allowing for densities larger than  $\rho^* = (\ell + \sqrt{\ell})^{-1}$  only in HD.

### 3.3 Application: inference of rates

Here we present an algorithm to infer rates from observed density profiles. If a system is well-approximated by the hydrodynamic limit, we can use the following method to fully recover  $\alpha, \beta$  and  $\lambda$ , up to a constant reflecting the time scale of the process, and thereby determine the system's location in the phase diagram:

1. **Fixing a time scale:** Since  $(\alpha, \beta, \lambda)$  are only determined up to a multiplicative constant, we may without loss of generality pick a site  $x_0 \in [0, 1]$  and assume  $\lambda(x_0) = 1$ . This is tantamount to fixing an arbitrary time scale.
2. **Inferring  $\lambda$ :** Fixing the time scale allows to compute the current according to (2) as  $J = \rho(x_0)G(\rho(x_0))$ . Whence for any  $x \in [0, 1]$ :

$$\lambda(x) = \frac{J}{\rho(x)G(\rho(x))}.$$

3. **Estimating  $\alpha, \beta$ :** Inverting (4) and (8) yields entrance and exit rates

$$\alpha = \frac{J}{1 - \ell\rho_0} \quad \text{and} \quad \beta = \frac{J}{\rho_1^+}.$$

An example application of this rate inference algorithm is illustrated in **Fig. 4**, which shows a significant improvement over the naive estimator  $\lambda = 1/\rho$  considered in [11]. A more refined analysis of the algorithm's performance, error propagation, and discrete lattice effects is in progress.

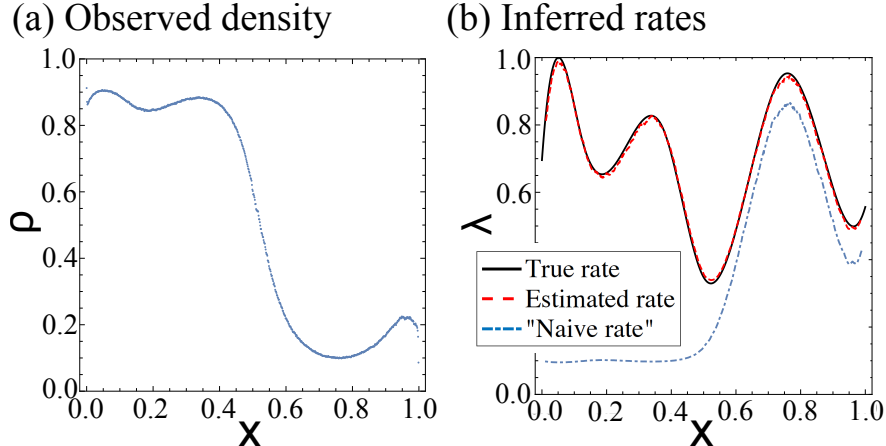


**Fig. 4: Rate Inference.** (a) Simulated density for  $\alpha = \beta = \ell = 1$ . (b) Applying our inference algorithm to simulated data recovers the underlying rate to high accuracy for all sites. In contrast, the naive estimator (which assumes no collision between particles) suffers from minor inaccuracy in low density regions, and is completely unable to reconstruct high density regions.

## 4 Future perspectives

The theory presented here demonstrates how the behavior of complex non-equilibrium particle systems like the inhomogeneous  $\ell$ -TASEP can be completely analyzed in the hydrodynamic limit. The results have practical implications for applications modeled by such systems. For example, investigating the regimes in which specific genes operate during translation can help to uncover the limiting factors for the overall rate of protein synthesis, which is a key quantity of biological interest. We are currently working on extending our approach to even more general TASEP models, incorporating bidirectional jump rates (ASEP) as well as birth and annihilation, which are relevant to DNA transcription and molecular transport.

## Appendix

### A The hydrodynamic limit of the inhomogeneous $\ell$ -TASEP

We derive here the hydrodynamic limit of the open-boundaries inhomogeneous  $\ell$ -TASEP. To do so we exploit a representation of its dynamics in terms of another interacting particle system, the so-called zero range process (ZRP), whose hydrodynamics can be found explicitly.

#### A.1 Reduction to periodic boundaries and mapping to the ZRP

The purpose of the hydrodynamic limit is to describe the local evolution of the macroscopic particle density in the large system limit. As such, it does not explicitly rely on the precise formalism by which particles enter and exit the lattice at the boundaries (which will only later be needed to impose boundary conditions on the resulting PDE). In particular, we are free to choose periodic boundary conditions for our limiting procedure without changing the resulting PDE [33]. This has the advantage of preserving the total number of particles, which is essential for establishing the correspondence between TASEP and ZRP. In the following, we thus consider the  $\ell$ -TASEP with

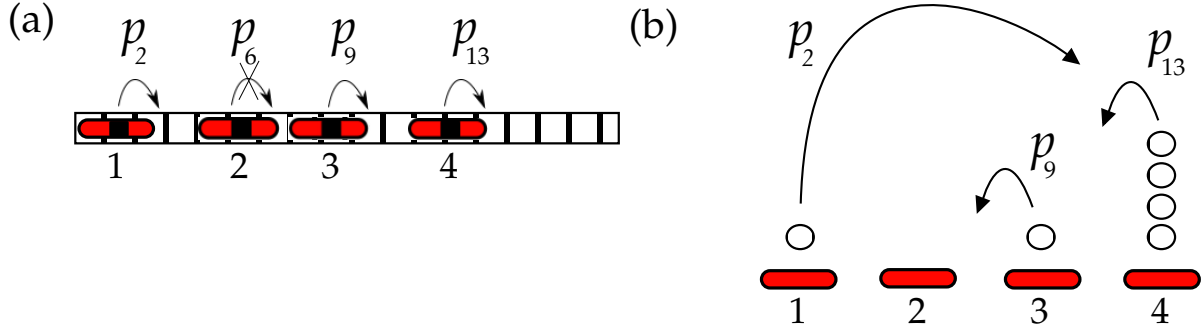


**Fig. 5: Correspondence between inhomogeneous  $\ell$ -TASEP and the ZRP.**  $\ell$ -TASEP particles (red) correspond to ZRP sites, and holes (empty squares) become ZRP particles.

$M$  particles on a *ring* of  $N$  sites jumping to the right at rate  $p_i$ , and take  $M, N \rightarrow \infty$  while  $M/N$  remains constant.

The ZRP is now obtained by reversing the roles of holes and particles: It consists of  $N - M\ell$  particles (corresponding to the  $N - M\ell$  holes in the TASEP) distributed across  $M$  sites (matching the TASEP particles)  $\{1, \dots, M\}$ , with multiple particles allowed to stack up on the same site. A ZRP configuration  $(\xi_{i,t})_{1 \leq i \leq M}$  describes the number of particles  $\xi_{i,t}$  at each site  $i \in \{1, \dots, M\}$  and time  $t$ , and can be seen as a representation of spacings between particles  $i$  and  $i + 1$  in the TASEP.

As a result, the TASEP dynamics are translated into ZRP dynamics as follows: If a site  $i$  at time  $t$  is occupied by at least one particle, then the topmost particle jumps to the left with rate  $m_{i,t} = p_{k(i,t)}$ , where  $k(i,t)$  is the position of the  $i$ th TASEP particle (see formula (11) below) at time  $t$ . This jump occurs regardless of whether the destination site is occupied or not. That is, neither exclusion nor long range interactions are present, which will be key to establishing the hydrodynamic limit.

The correspondence between TASEP and ZRP states described above is so far only determined up to rotations of the TASEP lattice, hence we introduce one further variable  $\xi_{0,t} \in \{1, \dots, N\}$  to trace the position of particle 1. More explicitly, at time  $t$ , TASEP particle  $i$  is located at site

$$k(i,t) = \sum_{j=0}^{i-1} \xi_{j,t} + \ell(i-1) \quad (11)$$

on the TASEP ring. An illustration of this correspondence is given in **Fig. 5**.

## A.2 The hydrodynamic limit of the ZRP

The connection between the TASEP and the ZRP has been fruitfully used to derive hydrodynamic limits for homogeneous systems [33,34]. Here we generalize this approach to heterogeneous lattices and supply appropriate boundary conditions to the PDE, which become necessary when working with open rather than periodic boundaries.

We start with the master equation associated with the ZRP:

$$\partial_t \xi_{i,t} = m_{i+1,t} z_{i+1,t} - m_{i,t} z_{i,t}, \quad (12)$$

where  $z_{i,t} = \mathbb{P}(\xi_{i,t} > 0)$  is the probability that site  $i$  is non-empty at time  $t$ . Our goal is to identify a PDE that describes the limit of (12) under Euler scaling, i.e., on time scale  $at$  and spatial scale  $ia$ . Denoting these scaled variables as  $t$  again in time and  $x, y$  in space such that  $k = \lfloor x/a \rfloor$  and

$i = \lfloor y/a \rfloor$ , the relation (11) between  $k, i$  and  $t$  lifts directly to a continuum relation between  $x, y$  and  $t$ . More precisely,

$$\begin{aligned} x(y, t) &= ak(i, t) = a \left[ \sum_{j=0}^{i-1} \xi_{j,t} + \ell(i-1) \right] \\ &= \int_0^y c(u, t) \, du - \frac{a}{2} [c(y, t) - c(0, t)] + \ell(y - a) + O(a^2). \end{aligned} \quad (13)$$

Assuming the existence of a continuously differentiable rate function  $\lambda$  such that  $\lambda(x) = p_k$ , the master equation (12) becomes

$$\begin{aligned} a\partial_t c(y, t) &= \lambda(x(y+a, t))z(y+a, t) - \lambda(x(y, t))z(y, t) \\ &= a\partial_y [\lambda(x(y, t))z(y, t)] + \frac{a^2}{2} \partial_{yy} [\lambda(x(y, t))z(y, t)] + O(a^3) \end{aligned} \quad (14)$$

where  $c(y, t)$  and  $z(y, t)$  are the continuum limits of  $\xi_{i,t}$  and  $z_{i,t}$ , respectively. Under local stationarity [26], we may replace  $z$  in (14) using the fugacity-density relation  $z = c(1+c)^{-1}$  to obtain the final hydrodynamic limit of the inhomogeneous ZRP as

$$\partial_t c = \partial_y \left( \lambda \frac{c}{1+c} \right) + \frac{a}{2} \partial_{yy} \left( \lambda \frac{c}{1+c} \right).$$

To derive the corresponding PDE for the TASEP, we recognize that particle densities are related by  $\rho = (c + \ell)^{-1}$  and change coordinates according to (13). This yields

$$\partial_t \rho = -\partial_x [\lambda(x)\rho G(\rho)] - \frac{a}{2} \partial_{xx} [\lambda(x)G(\rho)] + O(a^2), \quad (15)$$

where  $G(\rho) = \frac{1-\ell\rho}{1-(\ell-1)\rho}$ .

## B Phase diagram analysis

We now use (15) to provide a detailed derivation of the phase diagram described in Section 2.3.

### B.1 Reduction to conservation law

Solutions of (15) converge locally uniformly (under mild conditions on  $\lambda$ , see Section B.4) to viscosity solutions of the scalar conservation law

$$\partial_t \rho(x, t) = -\partial_x \underbrace{[\lambda(x)H(\rho(x, t))]}_{J(\rho(x, t), x)}, \quad (16)$$

where  $H(\rho) = \rho G(\rho)$ , which thus determines the phase diagram in the hydrodynamic regime. Setting  $\partial_t \rho = 0$  identifies the stationary profiles of the TASEP as distributions satisfying

$$J(\rho, x) = J_c \quad (17)$$

where  $J_c = J_c(\alpha, \beta, \lambda) \in [0, J_{\max}]$  is at most the transport capacity

$$J_{\max} = \min_{x \in [0, 1]} \max_{\rho \in [0, 1/\ell]} J(\rho, x) = \frac{\lambda_{\min}}{(1 + \sqrt{\ell})^2}$$

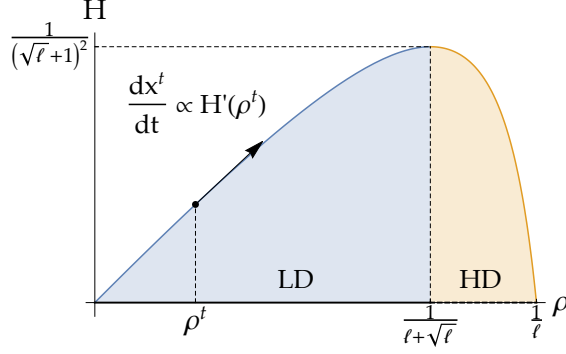


**Fig. 6:**  $H(\rho)$  and its effect on characteristic speeds. The rate-normalized flux  $H(\rho) = J(\rho, x)/\lambda(x)$  is depicted in blue, with characteristic velocity of  $x^t$  indicated. If  $J(\rho^0, x^0) < J_{\max}$ , the characteristic density  $\rho^t$  stays within the regions marked LD or HD, depending on the sign of  $\rho^0 - (\ell + \sqrt{\ell})^{-1}$ . Otherwise,  $\rho^t$  may cross  $(\ell + \sqrt{\ell})^{-1}$  forcing the characteristic  $x^t$  to return to its origin  $x^0$  (see Section C).

of the lattice. Equation (17) has two solutions (see **Fig. 6**) of the form

$$\rho_{\pm}(x) = \frac{1}{2\ell} + \frac{J_c(\ell - 1)}{2\ell\lambda(x)} \pm \sqrt{\left(\frac{1}{2\ell} + \frac{J_c(\ell - 1)}{2\ell\lambda(x)}\right)^2 - \frac{J_c}{\ell\lambda(x)}},$$

any mixture of which may be a potential attractor picked by the system as  $t \rightarrow \infty$ . Deciding precisely which mixture dominates requires analysis of the characteristic curves.

## B.2 Solving the characteristic ODE

Denoting the characteristic curves by  $x^t$  and  $\rho^t$  with initial data  $x^0, \rho^0$ , their evolution is described by the system of ODE [35]

$$\frac{dx^t}{dt} = \lambda(x^t)H'(\rho^t), \quad (18)$$

$$\frac{d\rho^t}{dt} = -\lambda'(x^t)H(\rho^t), \quad (19)$$

where  $H'$  and  $\lambda'$  respectively denote the derivatives of  $H$  and  $\lambda$  with respect to their arguments. The solutions are easily verified to be

$$\begin{aligned} x^t &= F^{-1}(t) \\ \rho^t &= H^{-1}\left(\frac{J(\rho^0, x^0)}{\lambda(x^t)}\right) \end{aligned} \quad (20)$$

as long as  $J(\rho^0, x^0) \in [0, J_{\max}]$ . The form of  $F$  follows from formally separating variables:

$$F(x) = \int_{x^0}^x \frac{1}{\lambda(y)H' \circ H^{-1}(J(\rho^0, x^0)/\lambda(y))} dy,$$

while  $H^{-1}(J(\rho^0, x^0)/\lambda(x^t))$  is understood to be the preimage compatible with  $\rho^0$ , see **Fig. 6**. In particular, if  $J(\rho^0, x^0) < J_{\max}$ , then for all  $t \geq 0$ ,

$$\frac{J(\rho^0, x^0)}{\lambda(x^t)} < \frac{1}{(1 + \sqrt{\ell})^2},$$

so  $\rho^t < \frac{1}{\ell + \sqrt{\ell}}$  for all  $t$  if  $\rho^0 < \frac{1}{\ell + \sqrt{\ell}}$ , while  $\rho^t > \frac{1}{\ell + \sqrt{\ell}}$  for all  $t$  if  $\rho^0 > \frac{1}{\ell + \sqrt{\ell}}$ . Hence, the sign of  $\frac{dx^t}{dt} = \lambda(x^t)H'(\rho^t)$  remains the same for all  $t$ , and any characteristic curve  $x^t$  starting at the left lattice boundary  $x^0 = 0$  or right lattice boundary  $x^0 = 1$  propagates towards the opposite end and fill the lattice entirely.

On the other hand, if  $J(\rho^0, x^0) > J_{\max}$ , then  $\frac{J(\rho^0, x^0)}{\lambda(x_{\min})} > \frac{1}{(1 + \sqrt{\ell})^2}$ , where  $x_{\min} = \arg \min_x \lambda(x)$ , so  $H^{-1}\left(\frac{J(\rho^0, x^0)}{\lambda(x_{\min})}\right) > \frac{1}{\ell}$ . Recalling (20) and noting that it is physically not possible to have  $\rho^t > \frac{1}{\ell}$ , we conclude that the characteristic curve  $x^t$  cannot reach  $x_{\min}$ . Indeed, it follows from (18) and (19) that at some critical time  $t_c$  before reaching  $x_{\min}$ , the characteristic curve  $x^t$  reverses direction while  $\rho^t$  crosses  $\arg \max_{\rho} H(\rho) = (\ell + \sqrt{\ell})^{-1}$ , resulting in  $x^t$  returning to its origin. **Fig. 2** and **Fig. 6** illustrate this behavior.

### B.3 Computing initial densities $\rho^0$

As a consequence of the above, determining phase transitions in the  $\alpha$ - $\beta$  phase diagram reduces to establishing regimes in which  $J(\rho^0, x^0)$  exceeds or falls short of  $J_{\max}$ , which in turn is equivalent to finding an expression for  $\rho^0$  in terms of  $\alpha$  and  $\beta$ . This is done by considering each lattice end separately and balancing currents:

#### B.3.1 The right lattice end $x^0 = 1$

As described in Section 2.3,  $\rho_1 = \rho(1)$  decomposes into a sum of two contributions, the periodic part  $\rho_1^+$  and the troughs  $\rho_1^-$  [23]. More explicitly,

$$\rho_1 = \frac{1}{\ell} \left[ (\ell - 1)\rho_1^- + \rho_1^+ \right].$$

Since the current  $J_c$  is a conserved quantity of the system, the local currents across the last lattice site, the second to last lattice site and within the last  $\ell$  sites must all be the same:

$$J_R := J(\rho_1, 1) = \beta\rho_1^+ = \lambda_1\rho_1^-. \quad (21)$$

Solving for  $\rho_1$  gives exactly  $\frac{1}{\ell}(1 - \frac{\beta}{\lambda_1})$ , as stated in Section 2.3. Consequently,  $J_R \leq J_{\max}$  iff

$$\beta < \beta^* = \frac{1}{2} \left[ \lambda_1 - \frac{\ell - 1}{(1 + \sqrt{\ell})^2} \lambda_{\min} - \sqrt{\left( \lambda_1 - \frac{\ell - 1}{(1 + \sqrt{\ell})^2} \lambda_{\min} \right)^2 - \frac{4\lambda_1 \lambda_{\min}}{(1 + \sqrt{\ell})^2}} \right].$$

#### B.3.2 The left lattice end $x^0 = 0$

Computing  $\alpha^*$  is more delicate as the effective jump rate is a combination of entrance rate and particle exclusion. To bypass this problem, we investigate the current of *holes* rather than particles, which is running in the opposite direction. With the loss of the particle-hole symmetry present in the simple 1-TASEP [37], the hole density  $\rho^h$  here assumes a more complicated form. It satisfies its own conservation law given by

$$\partial_{th} \rho^h = \partial_x [J^h(\rho^h, x)],$$

where

$$J^h(\rho^h, x) = \lambda(x)\rho^h \frac{1 - \rho^h}{1 + (\ell - 1)\rho^h}$$

and  $t^h = \ell t$  is the time scale of the holes, moving slower as their density is higher. Thus by balancing hole currents rather than particle currents at  $x^0 = 0$ , we obtain, noting that the effective exit rate (of holes) is still  $\alpha$  (as  $\ell$  holes need to accumulate for exiting to happen),

$$J^h(\rho_0^h, 0) = \alpha \rho_0^h. \quad (22)$$

Solving for  $\rho_0^h$  and using  $\rho_0^h = 1 - \ell \rho_0$ , we obtain  $\rho_0 = \alpha / [\lambda_0 + (\ell - 1)\alpha]$ . We define  $J_L := J(\rho_0, 0)$ , and determining  $\alpha$  such that  $J_L = J_{\max}$  gives  $\alpha^*$ .

## B.4 Phase transitions and profiles

Using the densities obtained from (21) and (22) in the characteristic curves (18) and (19) yields the HD and LD regimes for parameter configurations  $(\alpha > \alpha^*, \beta < \beta^*)$  and  $(\alpha < \alpha^*, \beta > \beta^*)$ , respectively. To describe the phase transition between HD and LD, we observe that for  $\alpha < \alpha^*$  and  $\beta < \beta^*$  both characteristic curves move into the lattice, meet, and move along a common shock with speed

$$v_{\text{shock}} = \frac{J_R - J_L}{\rho_r - \rho_l}$$

where  $\rho_l$  and  $\rho_r$  are the densities left and right of the shock. As  $\rho_r - \rho_l > 0$  as long as  $\alpha < \alpha^*$  and  $\beta < \beta^*$  (cf. **Fig. 6**),  $v_{\text{shock}} > 0$  iff  $J_R > J_L$ . That is, the slower current pushes the faster one past the lattice boundaries and dominates the stationary behavior of the system. The HD and LD regimes are thus separated by both incoming currents being of precisely equal magnitudes

$$J_L = \frac{\alpha(\lambda_0 - \alpha)}{\lambda_0 + (\ell - 1)\alpha} = \frac{\beta(\lambda_1 - \beta)}{\lambda_1 + (\ell - 1)\beta} = J_R.$$

Lastly, we can use the behavior of characteristic curves for  $J(\rho^0, x^0) > J_{\max}$  to describe stationary profiles in the MC regime ( $\alpha > \alpha^*$  and  $\beta > \beta^*$ ): Each characteristic curve reverses direction at a critical time  $t_c$  and returns to its respective lattice boundary, while the density  $\rho^t$  it carries transitions from  $\rho_-$  to  $\rho_+$  (on the left characteristic) or  $\rho_+$  to  $\rho_-$  (on the right characteristic). Since the reversal of directions occurs strictly before reaching  $x_{\min}$ , these characteristics provide density information on only part of the lattice. The remaining regions are determined by the simultaneously propagating rarefaction waves [35], which interpolate between  $x^t$  and the characteristic curve  $x_{\max}^t$  associated with  $J(\rho^0, x^0) = J_{\max}$  (see **Fig. 7**). Together, these observations combine to produce the high density and low density profiles to the left and right of  $x_{\min}$ , respectively, with critical current  $J_c = J_{\max}$ , as described in Section 2.3.

If  $\lambda$  has exactly one global minimum  $x_{\min}$  this description captures the density profile on the entire lattice. In the case of multiple global minima at  $\{x_{\min,1}, \dots, x_{\min,n}\}$  however, it describes  $\rho$  on  $[0, x_{\min,1}] \cup [x_{\min,n}, 1]$  only, leaving open fluctuations on the middle segment  $(x_{\min,1}, x_{\min,n})$ . Although unlikely to be encountered in practice, these singular rate functions exhibit interesting stochastic phenomena: The presence of high densities on the initial interval and low densities on the terminal one suggest the formation of a coexistence phase in-between. Indeed, the subsystem restricted to  $[x_{\min,1}, x_{\min,n}]$  may be regarded as a TASEP with entrance and exit rates  $\alpha = \beta = \lambda_{\min}/(1 + \sqrt{\ell})$ , positioning it at the triple point of the phase diagram, and computing the characteristics reveals one or multiple stationary shock fronts in the interior. Such macroscopic phenomenon in the homogeneous 1-TASEP has previously been associated on the microscopic level with a shock performing a random walk on the lattice with reflecting boundaries [40]. Numerical simulations seem to locate these shock around local maxima disproportionately often (cf. **Fig. 8**), which might reflect dependencies of its diffusivity on  $\lambda$ .

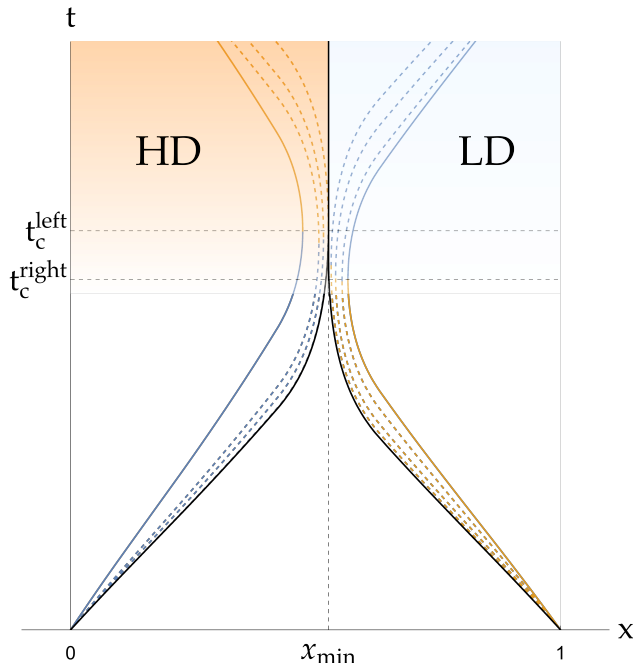


**Fig. 7: Propagation of characteristics in the MC regime.** If  $J(\rho^0, x^0) > J_{\max}$  the characteristic curves  $x^t$  (left and right colored solid curves) reverse directions at critical times  $t_c$  and return to their origin. At  $t_c$ , the density  $\rho^t$  switches from LD (blue) to HD (orange) (if associated with  $x^0 = 0$ ) or HD to LD (if associated with  $x^0 = 1$ , cf. **Fig. 6**). The same happens on all associated rarefaction waves (dashed curves), which interpolate between  $x^t$  and the stationary shock of  $x_{\max}^t$  (solid black curve).

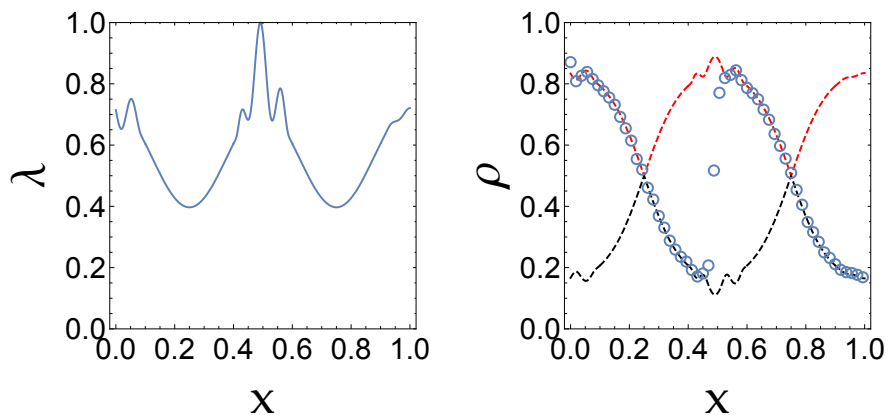


**Fig. 8: Illustration of branch switching (right plot) in the presence of two global minima in  $\lambda$  (shown left).** Circles are averaged counts over  $5 \times 10^7$  Monte-Carlo steps after  $10^7$  burn-in cycles on a lattice of size  $N = 2000$  with parameters  $\alpha = \beta = \ell = 1$ .

## C Boundary conditions

The computation of initial densities in Section B.2 yielded precise boundary values for  $x = 0$  in the LD regime and  $x = 1$  in the HD regime, respectively. Using the same principle of balancing currents, boundary conditions for all locations in the phase diagram can be computed. The results

**Table 1: Boundary conditions by phase.** Expected densities at the left ( $x = 0$ ) and right ( $x = 1$ ) end boundaries of the lattice.

Phase	$\rho_0$	$\rho_1^+$	$\rho_1^-$
LD	$\frac{\alpha}{\lambda_0 + (\ell - 1)\alpha}$	$\frac{1}{\beta} \left[ \frac{\alpha(\lambda_0 - \alpha)}{\lambda_0 + (\ell - 1)\alpha} \right]$	$\frac{1}{\lambda_1} \left[ \frac{\alpha(\lambda_0 - \alpha)}{\lambda_0 + (\ell - 1)\alpha} \right]$
HD	$\frac{1}{\ell} - \frac{1}{\ell\alpha} \left[ \frac{\beta(\lambda_1 - \beta)}{\lambda_1 + (\ell - 1)\beta} \right]$	$\frac{\lambda_1 - \beta}{\lambda_1 + (\ell - 1)\beta}$	$\frac{1}{\lambda_1} \left[ \frac{\beta(\lambda_1 - \beta)}{\lambda_1 + (\ell - 1)\beta} \right]$
MC	$\frac{1}{\ell} - \frac{1}{\ell\alpha} \left[ \frac{\lambda_{\min}}{(1 + \sqrt{\ell})^2} \right]$	$\frac{1}{\beta} \frac{\lambda_{\min}}{(1 + \sqrt{\ell})^2}$	$\frac{1}{\lambda_1} \frac{\lambda_{\min}}{(1 + \sqrt{\ell})^2}$

are listed in **Table 1**, which extend previous results obtained in [18] (who derived entries (1,1), (2,2) and (2,3) of **Table 1**). More precise information about the boundary layers can be gleaned from direct analysis of (15) rather than its limit (16).

## Acknowledgments

This research is supported in part by a Packard Fellowship for Science and Engineering. YSS is a Chan Zuckerberg Biohub investigator.

## References

- [1] MacDonald CT, Gibbs JH, Pipkin AC. Kinetics of biopolymerization on nucleic acid templates. *Biopolymers* **6**, 1–25 (1968).
- [2] Spitzer F. Interaction of Markov processes. *Advances in Mathematics* **5**, 246–290 (1970).
- [3] Miedema DM, Kushwaha VS, Denisov DV, Acar S, Nienhuis B, Peterman EJ, et al. Correlation Imaging Reveals Specific Crowding Dynamics of Kinesin Motor Proteins. *Physical Review X* **7**, 041037 (2017).
- [4] Kuan HS, Betterton MD. Motor protein accumulation on antiparallel microtubule overlaps. *Biophysical Journal* **110**, 2034–2043 (2016).
- [5] Chou T, Mallick K, Zia R. Non-equilibrium statistical mechanics: from a paradigmatic model to biological transport. *Reports on Progress in Physics* **74**, 116601 (2011).
- [6] Korkmazhan E, Teimouri H, Peterman N, Levine E. Dynamics of translation can determine the spatial organization of membrane-bound proteins and their mRNA. *Proceedings of the National Academy of Sciences* **114**, 13424–13429 (2017).
- [7] Shaw LB, Zia R, Lee KH. Totally asymmetric exclusion process with extended objects: a model for protein synthesis. *Physical Review E* **68**, 021910 (2003).
- [8] Ciandrini L, Stansfield I, Romano MC. Ribosome traffic on mRNAs maps to gene ontology: genome-wide quantification of translation initiation rates and polysome size regulation. *PLoS Computational Biology* **9**, e1002866 (2013).
- [9] Zia RK, Dong J, Schmittmann B. Modeling translation in protein synthesis with TASEP: A tutorial and recent developments. *Journal of Statistical Physics* **144**, 405–428 (2011).
- [10] Zur H, Tuller T. Predictive biophysical modeling and understanding of the dynamics of mRNA translation and its evolution. *Nucleic Acids Research* **44**, 9031–9049 (2016).
- [11] Dao Duc K, Song YS. The impact of ribosomal interference, codon usage, and exit tunnel interactions on translation elongation rate variation. *PLoS Genetics* **14**, e1007166 (2018).
- [12] Dao Duc K, Saleem ZH, Song YS. Theoretical analysis of the distribution of isolated particles in totally asymmetric exclusion processes: Application to mRNA translation rate estimation. *Physical Review E* **97**, 012106 (2018).
- [13] Basu A, Chowdhury D. Traffic of interacting ribosomes: effects of single-machine mechanochemistry on protein synthesis. *Physical Review E* **75**, 021902 (2007).
- [14] Szavits-Nossan J, Ciandrini L, Romano MC. Deciphering mRNA Sequence Determinants of Protein Production Rate. *arXiv preprint arXiv:170807678* (2017).
- [15] Mishra B, Chowdhury D. Interference of two codirectional exclusion processes in the presence of a static bottleneck: A biologically motivated model. *Physical Review E* **95**, 062117 (2017).
- [16] Shaw LB, Sethna JP, Lee KH. Mean-field approaches to the totally asymmetric exclusion process with quenched disorder and large particles. *Physical Review E* **70**, 021901 (2004).

- [17] Dong J, Schmittmann B, Zia RK. Inhomogeneous exclusion processes with extended objects: The effect of defect locations. *Physical Review E* **76**, 051113 (2007).
- [18] Lakatos G, Chou T. Totally asymmetric exclusion processes with particles of arbitrary size. *Journal of Physics A: Mathematical and General* **36**, 2027 (2003).
- [19] Kolomeisky AB, Schütz GM, Kolomeisky EB, Straley JP. Phase diagram of one-dimensional driven lattice gases with open boundaries. *Journal of Physics A: Mathematical and General* **31**, 6911 (1998).
- [20] Basu R, Sarkar S, Sly A. Invariant Measures for TASEP with a Slow Bond. *arXiv preprint arXiv:170407799* (2017).
- [21] Basu R, Sidoravicius V, Sly A. Last passage percolation with a defect line and the solution of the slow bond problem. *arXiv preprint arXiv:14083464* (2016).
- [22] Stinchcombe R, de Queiroz S. Smoothly varying hopping rates in driven flow with exclusion. *Physical Review E* **83**, 061113 (2011).
- [23] Chou T, Lakatos G. Clustered bottlenecks in mRNA translation and protein synthesis. *Physical Review Letters* **93**, 198101 (2004).
- [24] Greulich P, Schadschneider A. Phase diagram and edge effects in the ASEP with bottlenecks. *Physica A: Statistical Mechanics and its Applications* **387**, 1972–1986 (2008).
- [25] Liu M, Wang R, Hu MB, Jiang R, Gao Y. Synchronous asymmetric exclusion processes with an extended defect. *Physics Letters A* **374**, 1407–1413 (2010).
- [26] Kipnis C, Landim C. Scaling limits of interacting particle systems. vol. 320. Springer Science & Business Media. (2013).
- [27] Blythe RA, Evans MR. Nonequilibrium steady states of matrix-product form: a solver’s guide. *Journal of Physics A: Mathematical and Theoretical* **40**, R333 (2007).
- [28] Covert P, Rezakhanlou F. Hydrodynamic limit for particle systems with nonconstant speed parameter. *Journal of statistical physics* **88**, 383–426 (1997).
- [29] Rezakhanlou F. Hydrodynamic limit for attractive particle systems on 417-1417-1417-1. *Communications in Mathematical Physics* **140**, 417–448 (1991).
- [30] Seppäläinen T, et al. Existence of hydrodynamics for the totally asymmetric simple K-exclusion process. *The Annals of Probability* **27**, 361–415 (1999).
- [31] Benassi A, Fouque JP. Hydrodynamical limit for the asymmetric simple exclusion process. *The Annals of Probability* **15**, 546–560 (1987).
- [32] Derrida B, Domany E, Mukamel D. An exact solution of a one-dimensional asymmetric exclusion model with open boundaries. *Journal of Statistical Physics* **69**, 667–687 (1992).
- [33] Schönherr G, Schütz G. Exclusion process for particles of arbitrary extension: hydrodynamic limit and algebraic properties. *Journal of Physics A: Mathematical and General* **37**, 8215 (2004).

- [34] Schönherr G. Hard rod gas with long-range interactions: Exact predictions for hydrodynamic properties of continuum systems from discrete models. *Physical Review E* **71**, 026122 (2005).
- [35] Evans LC. *Partial Differential Equations*, Vol. 19 of Graduate Studies in Mathematics American Mathematical Society. Providence, Rhode Island: American Mathematical Society. (2010).
- [36] Lighthill MJ, Whitham GB. On kinematic waves. II. A theory of traffic flow on long crowded roads. *Proceedings of the Royal Society of London Series A, Mathematical and Physical Sciences* **229**, 317–345 (1955).
- [37] Derrida B, Evans MR, Hakim V, Pasquier V. Exact solution of a 1D asymmetric exclusion model using a matrix formulation. *Journal of Physics A: Mathematical and General* **26**, 1493 (1993).
- [38] Ingolia NT, Ghaemmaghami S, Newman JR, Weissman JS. Genome-wide analysis in vivo of translation with nucleotide resolution using ribosome profiling. *Science* **324**, 218–223 (2009).
- [39] Tuller T, Carmi A, Vestsigian K, Navon S, Dorfan Y, Zaborske J, et al. An evolutionarily conserved mechanism for controlling the efficiency of protein translation. *Cell* **141**, 344–354 (2010).
- [40] Derrida B, Lebowitz J, Speer E. Shock profiles for the asymmetric simple exclusion process in one dimension. *Journal of Statistical Physics* **89**, 135–167 (1997).